Multi-frequency Teleseismic P-wave Back-projection of the 2025 Mw 8.8 Kamchatka Peninsula Earthquake

K. Tarumi[1,*] and K. Yoshizawa[1]

[1]Department of Earth & Planetary Sciences, Faculty of Science, Hokkaido University, Sapporo 060-0810, Japan.

[*]Corresponding author: tarumi.kotaro.jp@gmail.com

This is a preprint that is submitted to EarthArXiv. The original manuscript has been submitted to Earth and Planetary Science Letters.

Highlights

Multi-frequency Teleseismic P-wave Back-projection of the 2025 Mw 8.8 Kamchatka Peninsula Earthquake

Kotaro Tarumi, Kazunori Yoshizawa

- Source process of the 2025 Kamchatka earthquake is imaged by P-wave back-projection.
- P-wave radiation varies with frequency range.
- Low-frequency P-waves suggest shallow near-trench sources implying dynamic overshoot.
- High-frequency P-waves are emitted where rupture and slip velocities change abruptly.
- Source regions of the 1952 Mw 9.0 and 2025 Mw 8.8 Kamchatka events are comparable.

Multi-frequency Teleseismic P-wave Back-projection of the 2025 Mw 8.8 Kamchatka Peninsula Earthquake

Kotaro Tarumi[a], Kazunori Yoshizawa[a]

[a]*Department of Earth and Planetary Sciences, Faculty of Science, Hokkaido University, Sapporo, 060-0810, Japan*

Abstract

A great megathrust earthquake with moment magnitude Mw 8.8 struck off the Kamchatka Peninsula on July 29, 2025, generating a Pacific-wide tsunami and rupturing a segment of the Kuril–Kamchatka subduction zone that has repeatedly hosted M9-class earthquakes. We apply multi-frequency teleseismic P-wave back-projection (BP) analysis using six frequency bands spanning 0.003–2.0 Hz to investigate the frequency-dependent rupture process of this event. The BP images reveal four distinct radiation episodes (E0–E3) within 180 s, during which the main rupture propagated southwestward along the plate interface and produced two prominent shallow near-trench sources. Low-frequency (LF; 0.02–0.5 Hz) P-wave radiation highlights these shallow near-trench episodes, possibly reflecting dynamic overshoot similar to the 2011 Tohoku earthquake. In contrast, higher-frequency (HF: 0.1–2.0 Hz) radiation illuminates a patch at the downdip edge of the near-trench episode (E3), as well as deeper sources in the initial and intermediate stages. The apparent migration speed of the radiating areas increases from about 1.0 to 2.0–2.5 km/s, and HF bursts coincide with rapid growth in the LF radiating area, suggesting abrupt changes in rupture and slip velocities. These findings further imply that the 2025 Kamchatka earthquake likely re-rupture source regions comparable to those of the 1952 Mw 9.0 event.

Keywords: Kamchatka, megathrust earthquake, P-wave radiation, back projection, source process, high frequency

1. Introduction

On July 29, 2025, a megathrust earthquake with moment magnitude M_w 8.8 occurred off the eastern coast of the Kamchatka Peninsula, along the Kuril–Kamchatka subduction zone (e.g., USGS, 2025b) (Fig.1 (a)). The U.S. Geological Survey (USGS) and the Global Centroid Moment Tensor project (GCMT; Dziewonski et al., 1981; Ekström et al., 2012) reported a low-angle thrust faulting mechanism for this event (USGS, 2025b). The resulting tsunami was recorded across the Pacific Ocean, including Japan, Hawaii, and Chile (e.g., Ruiz-Angulo et al., 2025), with maximum runup heights exceeding 15 m along the Kamchatka coast (Emelyanova, 2025).

The aftershock distribution in the first two weeks following the mainshock shows a paucity of events near the hypocentral region and extensive activity in southeastern Kamchatka and around Paramushiru (Fig. 1 (a)). In addition, the azimuthal patterns of observed surface-wave amplitudes (Fig. 1 (b,c)), corrected for geometrical spreading, exhibit strong enhancement toward the southwest relative to the point-source radiation patterns. These observations imply that the source rupture propagated southwestward. A previous megathrust earthquake with M_w 9.0 occurred in 1952 near the hypocenter of the 2025 event (e.g., Ben-Menahem and Toksöz, 1963; Kanamori, 1976). Ben-Menahem and Toksöz (1963) inferred southwestward rupture propagation from a directivity analysis of surface waves. Using historical tsunami records, Johnson and Satake (1999) estimated a static slip distribution with large slip south of the hypocenter. Although Johnson and Satake (1999) located these large-slip areas along the deeper portion of the plate interface, alternative models invoking significant shallow slip have been proposed to explain tsunami deposits (MacInnes et al., 2010). For the 2025 M_w 8.8 event, kinematic source models based on seismic waveforms (USGS, 2025b; Yagi et al., 2025) and tsunami observations (Ruiz-Angulo et al., 2025) reveal southwestward rupture starting at the hypocenter and suggest high slip rates along the shallow portion of the plate interface. Thus, both the 1952 and 2025 great earthquakes may have ruptured similar shallow segments southeast of the peninsula.

Frequency-dependent seismic radiation during large subduction-zone thrust earthquakes has

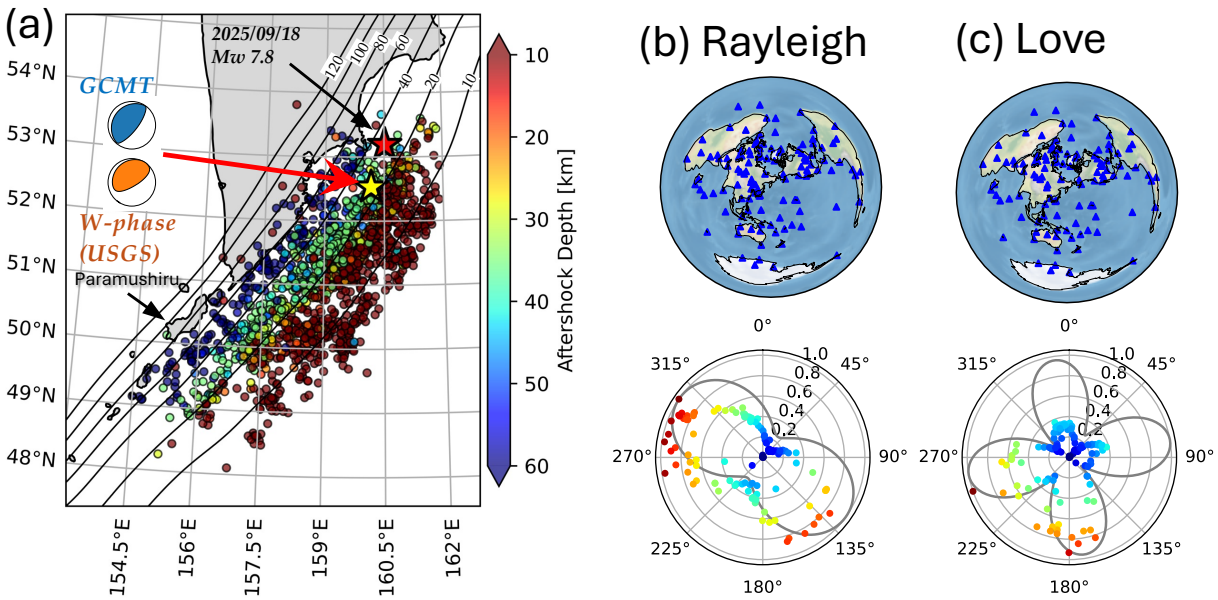

Figure 1: (a) Map of the study area and aftershock distribution during the first two weeks after the mainshock. Colors of circles denote the event depths. Blue and orange beachballs represent the GCMT (Ekström et al., 2012) and USGS W-phase MT (USGS, 2025b) of the Mw 8.8 event, respectively. Yellow and red stars indicate the epicenter of the Mw 8.8 mainshock and the largest aftershock (Mw 7.8) on September 18, 2025, (USGS, 2025b,a). Black contour lines indicate the depth of the subducting slab taken from the Slab 2.0 model (Hayes et al., 2018). (b, c) Azimuthal amplitude variations of Rayleigh and Love waves. The top panel shows the station distribution used in these amplitude measurements. The lower panels show the normalized amplitudes. Colors of the dots indicate the observed amplitudes. Gray solid lines represent the point source radiation patterns calculated from the GCMT solution.

been documented in several recent events (e.g., Ishii, 2011; Koper et al., 2011; Yagi et al., 2012; Okuwaki et al., 2014; Dhakal et al., 2022). For the 2011 Tohoku earthquake, high-frequency (HF) P-waves originated primarily from deeper parts of the source region, whereas low-frequency (LF) sources were concentrated near the trench (e.g., Ishii, 2011; Koper et al., 2011; Yagi et al., 2012), providing important clues for understanding the underlying rupture processes. For the 2010 Chile earthquake, Okuwaki et al. (2014) found that HF sources were located at the edges of large-slip areas (i.e, asperities), suggesting that abrupt changes in slip velocity generate HF radiation. These studies indicate that simultaneously imaging both LF and HF sources is essential for understanding the source process of megathrust earthquakes, including their complex rupture behavior.

In this study, we apply multi-frequency teleseismic P-wave back-projection analysis to the

2025 M_w 8.8 Kamchatka earthquake to investigate its frequency-dependent P-wave radiation. This approach allows us to resolve the relationship between LF and HF sources and to discuss rupture kinematics along the Kamchatka–Kuril plate interface. We also compare the spatial distribution of P-wave radiation with that obtained for the 1952 M_w 9.0 event to examine the relationship between the recent megathrust rupture and historical great earthquakes in this region.

2. Data: Multi-frequency Teleseismic P-wave

For teleseismic P-wave analyses, we used seismic stations located at epicentral distances between 30° and 90°. The data processing followed Tarumi and Yoshizawa (2025) and was applied to six frequency bands of 0.003–1.0 Hz, 0.02–0.1 Hz, 0.03–0.3 Hz, 0.05–0.5 Hz, 0.1–1.0 Hz, and 0.3–2.0 Hz. The broadband range (0.003–1.0 Hz) is useful for capturing the overall P-wave radiation process. As a reference, our multiple-frequency approach allows us to investigate both macroscopic patterns and finer-scale complexity of the P-wave radiation simultaneously.

Firstly, we used a cross-correlation-based waveform selection method for the onsets of teleseismic P-waves within time windows spanning 10 s before to 10 s after the reference P-wave travel times from ak135 (Kennett et al., 1995). We calculated the normalized correlation coefficient (NCC) for all station pairs and constructed groups of traces with NCC $>$ 0.7. We then selected the largest group for the back-projection analyses. Secondly, we corrected P-wave polarities using the signs of the NCCs and refined relative travel times from the lag corresponding to the maximum NCC. These processes were applied to each frequency band to reduce the influence of multi-scale structural heterogeneities.

Figs. 2 and S1–5 show the retained P-wave data in each frequency band. All datasets used for the back-projection show good azimuthal coverage, allowing us to achieve stable imaging resolution (Fukahata et al., 2014) (Figs. 2 (a) and S1–5 (a)).

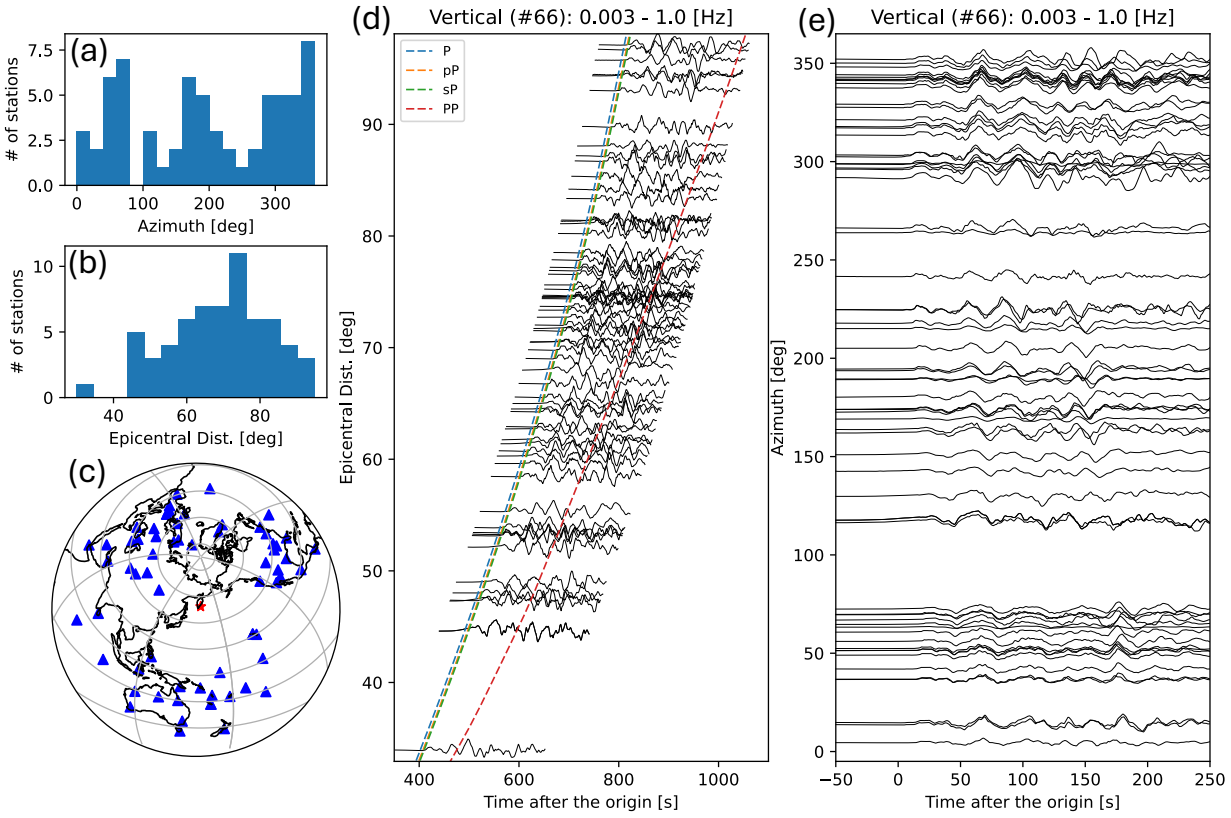

Figure 2: Teleseismic P-wave dataset for 0.003–1.0 Hz band. (a, b) Histograms of station azimuth and epicentral distance. (c) Station distribution. (d) Teleseismic P-wave traces used in this frequency range, aligned by the epicentral distance. (e) Same as (d), but sorted by station azimuth.

3. Method: LQT Back-projection

We used the LQT back-projection (BP) method (Tarumi and Yoshizawa, 2025) to image the frequency-dependent P-wave radiation. In this section, we briefly summarize the BP implementation adopted in this study.

The back-projection method was originally developed to estimate the rupture process of large earthquakes (Ishii et al., 2005, 2007). It has also been applied to tracking aftershocks hidden within the seismic disturbances of large earthquakes (Kiser and Ishii, 2013), imaging tsunami propagation and the associated source process (Mizutani and Yomogida, 2022), and resolving explosive eruption sequences (Tarumi and Yoshizawa, 2023).

The BP procedure is based on a slant-stacking approach that time-reverses a target phase (e.g.,

Table 1: Grid sizes used in the BP analysis for each frequency range.

Frequency [Hz]	Grid interval [°]
0.02–0.1 Hz	0.1°
0.03–0.3 Hz & 0.05–0.5 Hz	0.05 °
0.003–1.0 Hz & 0.1–1.0 Hz	0.025 °
0.3–2.0 Hz	0.015 °

P-wave) into a potential source region, whose schematic illustration are shown in Fig. S6 (a) . In the original BP framework, vertical-component seismograms are typically used, because teleseismic P-waves are predominantly recorded on the vertical component. However, the teleseismic P-waves are observed in the vertical-radial plane due to the non-vertical incidence angle. We therefore rotate the three-component seismograms into the LQT coordinate system (Fig. S6 (b)), which has been widely used in receiver function studies (e.g., Vinnik, 1977), and stack the L-component data aligned with the theoretical P-wave incidence direction (LQT-BP; Tarumi and Yoshizawa, 2025). To suppress sidelobes in the stacked BP images while enhancing coherent energy, we adopt the N-th root stacking method (Rost and Thomas, 2002) with $N = 4$ in this study, which was determined empirically.

The potential source grid used in this study is defined along the subducting slab surface modeled by Hayes et al. (2018). In most BP studies, seismic sources are assumed to lie on a single depth plane (e.g., Ishii et al., 2007; Koper et al., 2011). However, because the Mw 8.8 Kamchatka earthquake occurred along the Kamchatka–Kuril subduction zone, we instead constrain the potential P-wave sources a priori to a fault surface coincident with the slab geometry. To construct this potential source surface, we resample spatial points on the Slab 2.0 model (Hayes et al., 2018) (Fig. S7). The grid spacing in this resampled surface is varied for each frequency band, roughly based on the wavelength in that band, and the adopted values are listed in Table 1.

For the BP calculations, we use the AK135 model (Kennett et al., 1995) to compute theoretical P-wave travel times and incidence angles from each potential source to each station.

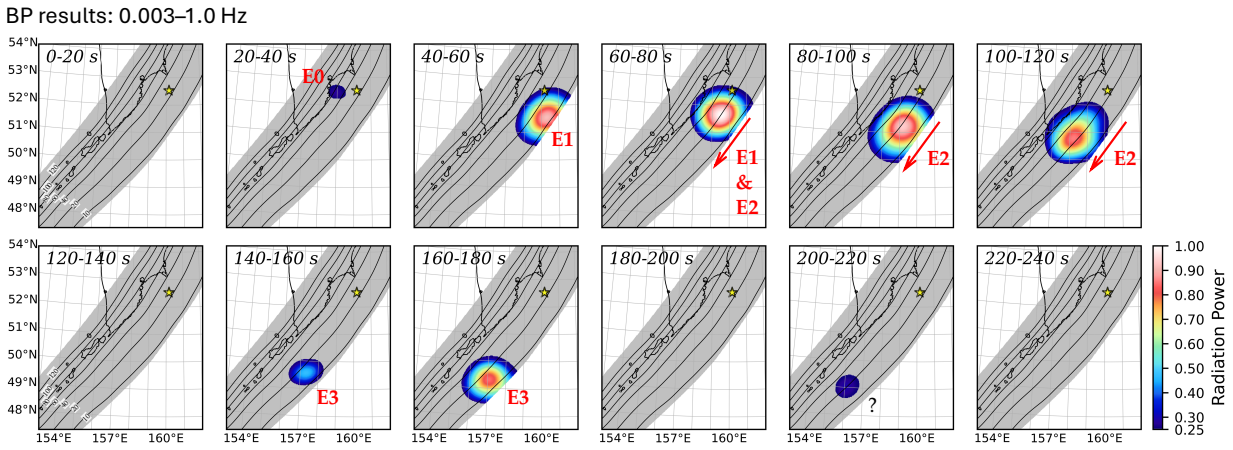

Figure 3: Back-projection snapshots with 20-s interval for 0.003–1.0 Hz. For clarity, grids with intensities lower than 0.25 are masked. Yellow stars show the epicenter of this earthquake (USGS, 2025b). Black contour lines delineate the depth of the subducting slab extracted from the Slab 2.0 model (Hayes et al., 2018), whose depths are specifically shown in the initial time panel. Red characters (E0-E3) highlight the interpreted episodes. Red arrows indicate the migration directions of the P-wave radiation areas.

4. Results and Discussions

4.1. Frequency-dependent P-wave radiation

Snapshots of the back-projection (BP) images at 20 s intervals are shown in Fig. 3 for 0.003–1.0 Hz, Fig. 4 for the three lower-frequency ranges (0.02–0.1 Hz, 0.03–0.3 Hz, and 0.05–0.5 Hz), and Fig. 5 for the two higher-frequency ranges (0.1–1.0 Hz and 0.3–2.0 Hz). To illustrate the spatiotemporal relationship between the low-frequency (LF) and high-frequency (HF) sources, Fig. 6 shows the temporal evolution of P-wave radiation in all frequency bands, projected onto the slab surface.

The overall P-wave radiation (Fig. 3) can be divided into four distinct episodes (E0–E3) during 180 s, including two stages of near-trench radiation. The P-wave radiation starts near the epicenter at depth and lasts for about 0–40 s (E0). The subsequent episode at 40–70 s radiates intense P-waves near the trench in eastern Kamchatka, representing the first major radiation episode (E1). During 70–120 s, the main radiation region migrates southwestward, constituting the second major episode (E2). Although the P-wave radiation temporarily weakens during 120–140 s, it reappears near the trench in southeastern Kamchatka and around Paramushiru Island during 140–180 s,

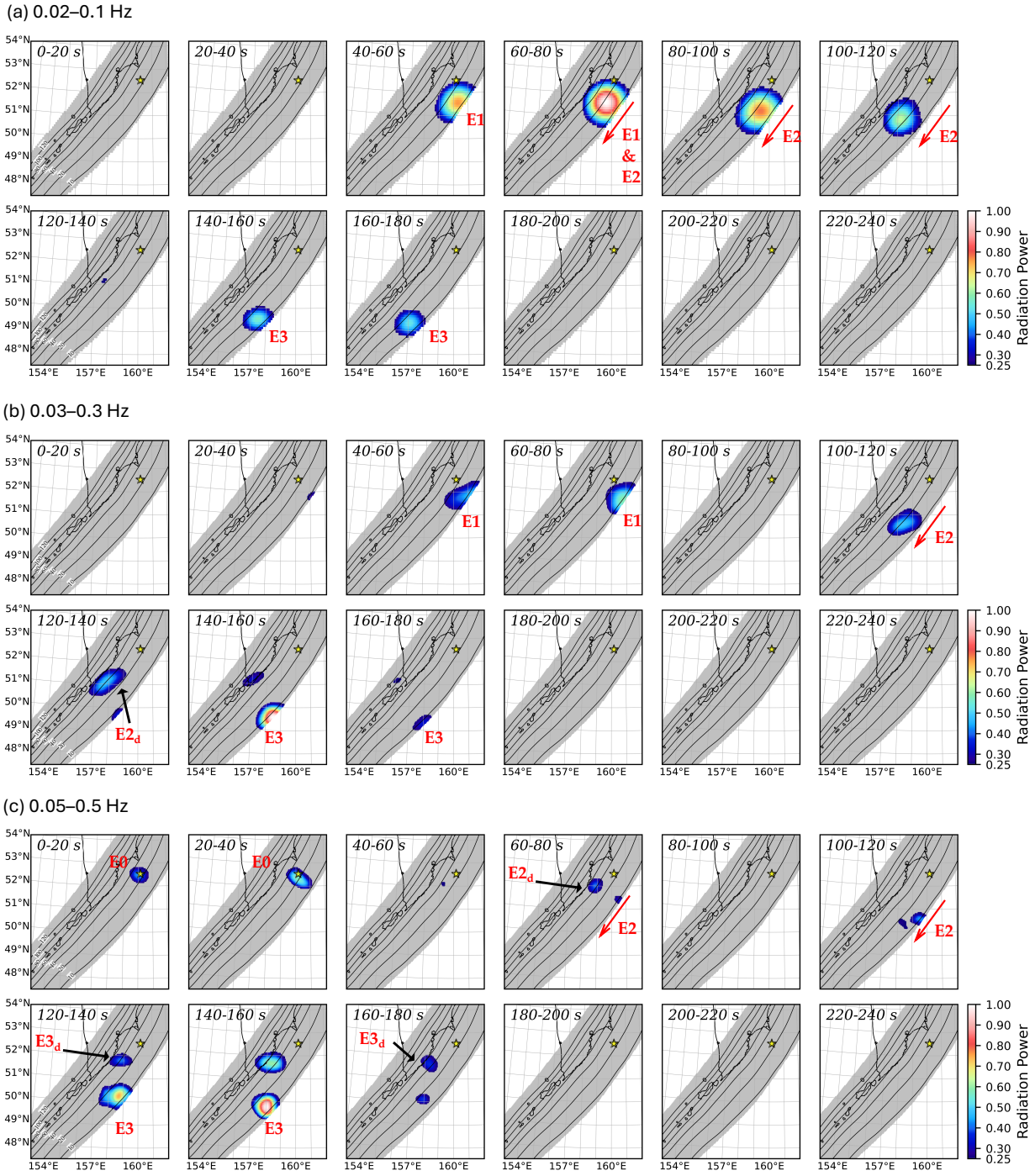

Figure 4: Same as Figure 3, but for the relatively lower frequency ranges (a: 0.02–0.1 Hz; b: 0.03–0.3 Hz; c: 0.05–0.5 Hz).

corresponding to the third major radiation stage (E3). The timing of these episodes is summarized in Fig. 6(a), and similar patterns are observed in the narrower frequency bands, although with different relative amplitudes (Figs. 4 and 5). After 180 s from the origin time (OT), additional P-wave radiation emerges south of Paramushiru Island at around 210 s (Figs. 3 and 6(a)), which is not present in any of the narrower bands (Figs. 4, 5, and 6(b–d)).

In the following two subsections, we separately describe the LF and HF P-wave radiation images and compare our BP images with the kinematic inversion models.

4.1.1. Low-frequency P-wave radiation

Fig. 4 displays the BP results for (a) 0.02–0.1 Hz, (b) 0.03–0.3 Hz, and (c) 0.05–0.5 Hz. The lowest-frequency band (Fig. 4 (a)) shows P-wave source distributions broadly similar to the overall P-wave radiation (Fig. 3), except that neither the initial episode E0 nor the late emission at 210 s appears.

The results of 0.03–0.3 Hz and 0.05–0.5 Hz (Fig. 4(b, c)) are also consistent with the overall radiation history (Fig. 3), but they highlight E3 as an intense shallow source region near Paramushiru Island (Fig. 4 (b, c)). In addition, these relatively higher low-frequency bands (0.03–0.3 Hz and 0.05–0.5 Hz) exhibit radiation from deeper portions of the subducting plate during the southwestward rupture propagation (a deeper subepisode, E2d), coinciding with a temporary cessation of radiation in the lowest-frequency band (Figs. 3 and 4 (a)).

4.1.2. High-frequency P-wave radiation

The high-frequency (HF) P-wave BP images exhibit deeper radiation than the LF images, particularly for E0 and the deeper part of E2 (E2d in Fig. 5 (a, b)), although the 0.1–1.0 Hz band also shows a relatively shallow migration of the radiating region (Fig. 5 (a)). Furthermore, during 140–160 s, the HF energy is enhanced along the downdip (deep) edge of the E3 patch imaged by LF P-waves (Figs. 3 and 4). We refer to this HF patch as E3' (Fig. 5 (a, b)).

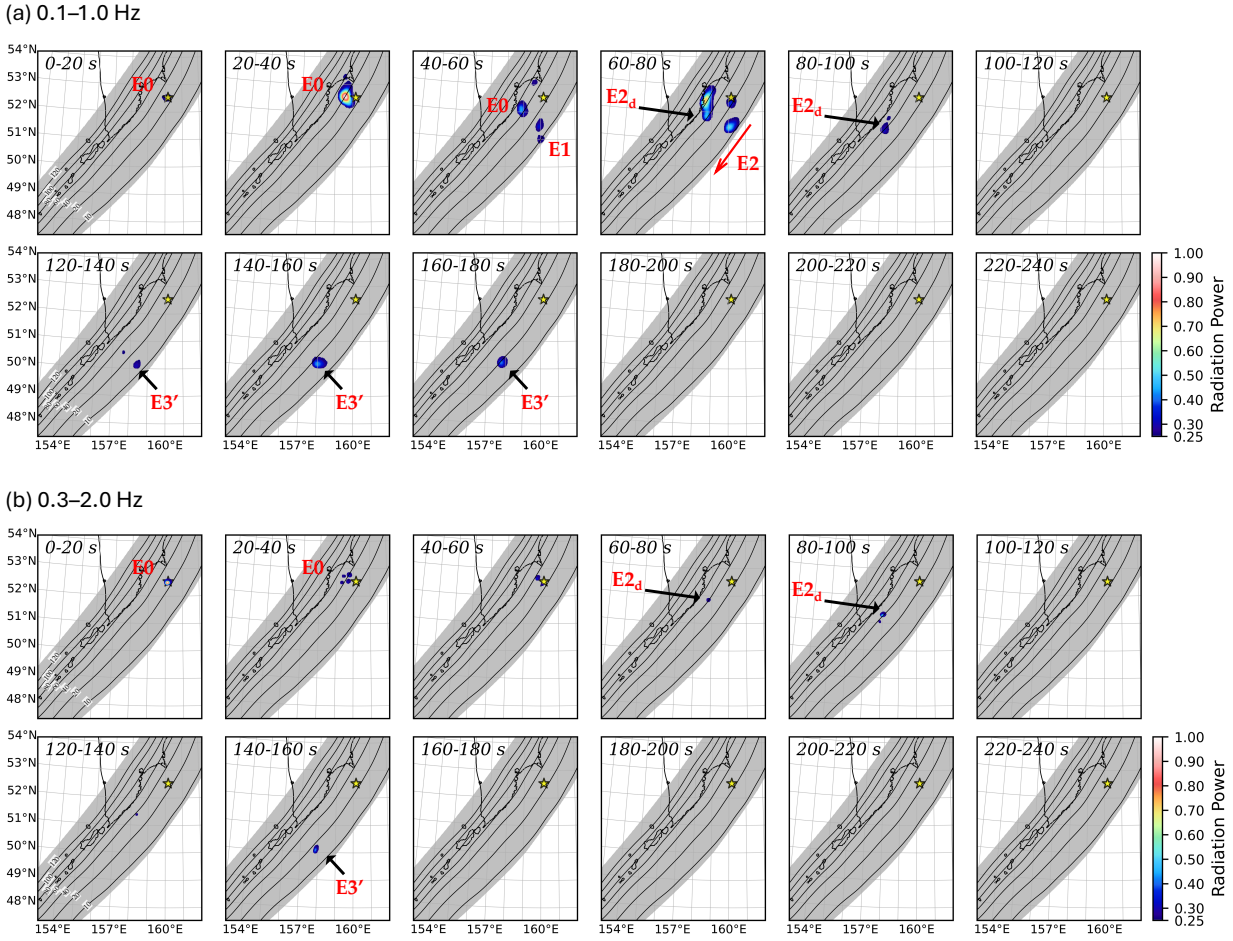

Figure 5: Same as Figure 3, but for the higher frequency ranges (a: 0.1–1.0 Hz; b: 0.3–2.0 Hz).

4.1.3. Comparison between our BP and seismic waveform inversion models

Our BP models (Figs. 3, 4, and 5) are generally consistent with previous inversion results (USGS, 2025b; Yagi et al., 2025). USGS (2025b) performed finite-fault inversion using teleseismic P and SH waves, long-period surface waves, and InSAR data, assuming three fault planes with different dip angles. Yagi et al. (2025) conducted potency-density tensor inversion (Shimizu et al., 2019; Yamashita et al., 2022), incorporating Green's-function uncertainties (Yagi and Fukahata, 2011) to fit teleseismic P-waves on a single fault plane, including relatively high-frequency components in the P-wave trains. In all three approaches, the southwestward rupture propagation is robust and is also supported by the azimuthal pattern of surface-wave amplitudes (Fig. 1(b, c)).

However, for E1 at 40–70 s after OT (Figs. 3 and 4), USGS (2025b) inferred only minor slip in this near-trench region, and Yagi et al. (2025) suggested that the near-trench area above the epicenter experienced significant slip at 110–140 s after OT. Furthermore, regarding the spatial distribution of radiation intensity and slip amount, USGS (2025b) and Yagi et al. (2025) indicated that episode E3 involves larger slip than E1, whereas our BP results for the broadband and lowest-frequency ranges (Figs. 3 and 4(a)) suggest comparatively stronger radiation during E1 and E2.

A P-wave BP analysis for 0.05–0.15 Hz by Yagi et al. (2025), which used the same fault plane as their inversion model, is in good agreement with our 0.03–0.3 Hz and 0.05–0.5 Hz results (Figs. 4(b, c) and 6(c, d)). In terms of radiation amplitude, the results of these two frequency ranges are also consistent with those inferred from the potency-density tensor inversions (Yagi et al., 2025). This suggests that the discrepancy in the timing and amplitude of E1 does not arise from differences in fault geometry, but rather from the different sensitivities and frequency ranges of BP and inversion analyses.

4.2. Insights into rupture characteristics

The source-migration speed, which provides an estimate of the rupture velocity, is on the order of 2.0–2.5 km/s based on the projected diagrams in Fig. 6. This apparent velocity, however, increases during the rupture process; the migration speed changes from about 1.0 km/s to 2.0 km/s between episodes E0/E1 and E2, and from 2.0 km/s to 2.5 km/s between E2 and E3 (Fig. 6), suggesting rupture acceleration. These timings of acceleration are also characterized by intense HF emission (Fig. 6), highlighting abrupt changes in rupture velocity.

In addition, the LF radiation begins to increase at these times (Fig. 6), and the leading edge of the LF source area is accompanied by HF radiation (E0 and E3'). If the LF radiation area is interpreted as an asperity, the HF emission may reflect rapid changes in the slip velocity at the asperity edge, as well as changes in the rupture velocity. Similar behavior around asperities has been reported for the 2010 M8.8 Chile earthquake using an alternative BP approach (hybrid BP) (Okuwaki et al., 2014) and for this Mw 8.8 Kamchatka event based on a teleseismic P-wave inver-

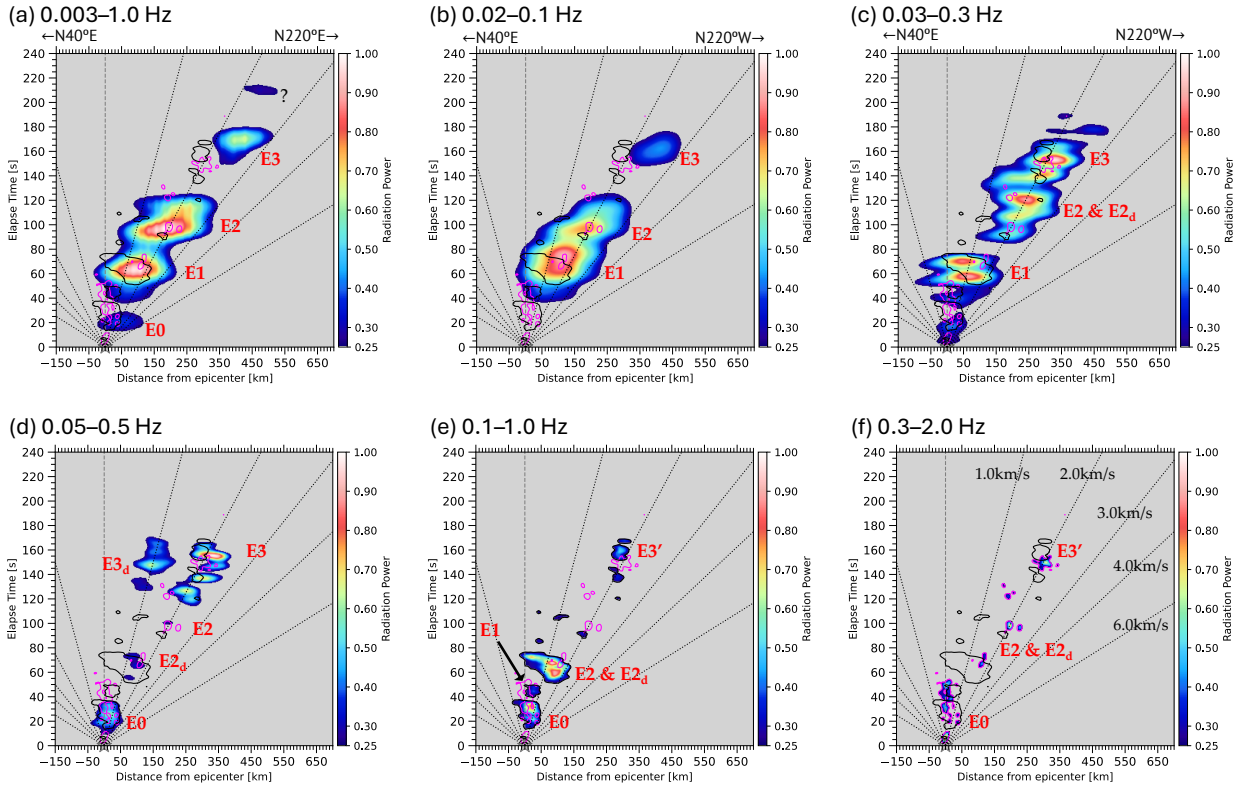

Figure 6: Temporal evolution of multi-frequency P-wave radiation projected onto the slab surface (a: 0.003–1.0 Hz; b: 0.02–0.1 Hz; c: 0.03–0.3 Hz; d: 0.05–0.5 Hz; e: 0.1–1.0 Hz; f: 0.3–2.0 Hz). Black and magenta contours represent the temporal evolution of BP power of 0.1–1.0 Hz and 0.3–2.0 Hz, respectively. Black dotted lines indicate the arrival times of rupture fronts with 1.0, 2.0, 3.0, 4.0, and 6.0 km/s. Black stars show the hypocenter. In each panel, the right-hand direction corresponds to N220°E.

sion (Yagi et al., 2025). Our results suggest that the HF P-waves in the 2025 Mw 8.8 Kamchatka earthquake are enhanced by abrupt transitions in both rupture and slip velocities.

We identify two distinct shallow near-trench episodes, E1 and E3 (Figs. 3 and 4). Although both are also captured by inversion studies (Yagi et al., 2025), E3 is more consistent with our BP images, which show intense P-wave radiation from the near-trench region (Figs. 3 and 4). A similar near-trench feature was inferred for the 2011 Tohoku earthquake by Yagi et al. (2012), and was interpreted as reflecting dynamic overshoot near the trench (Ide et al., 2011). Ide et al. (2011) also documented increased normal-fault earthquakes in that region, and comparable normal-fault activity has been reported for the 2025 Kamchatka event (Yagi et al., 2025). Therefore, the shallow LF radiation during E3 may likewise reflect dynamic overshoot along the trench (Oglesby et al.,

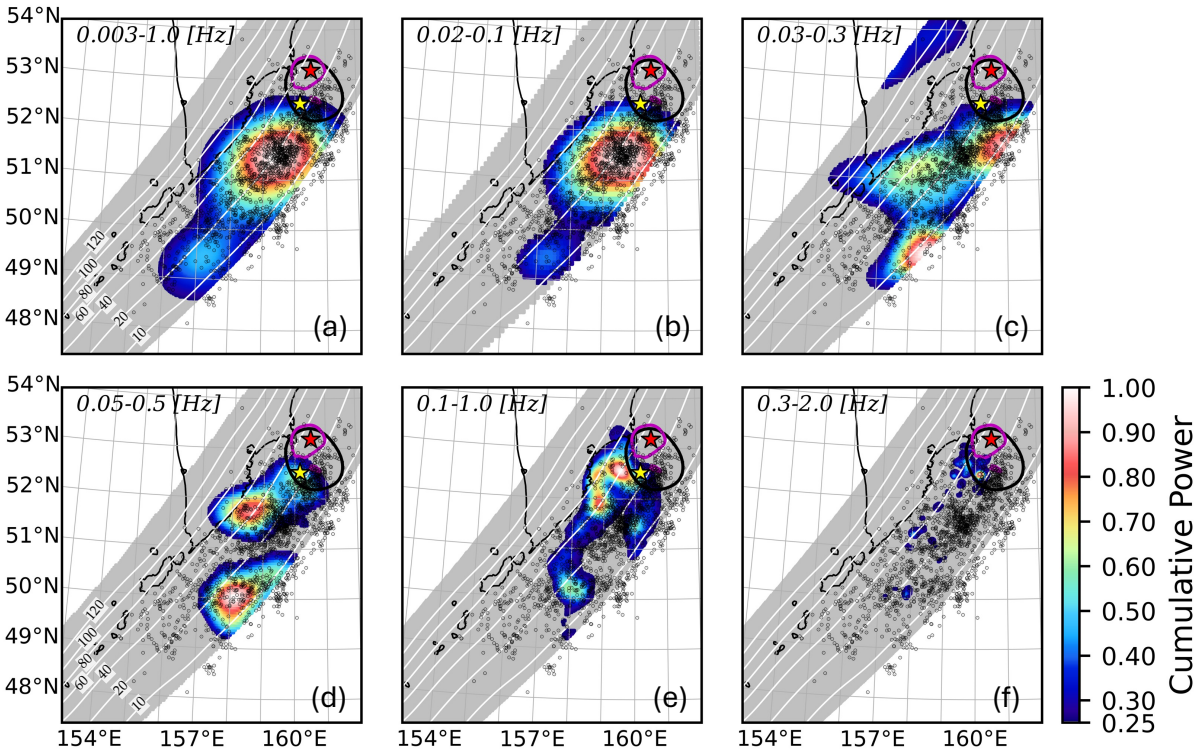

Figure 7: Spatial relationship among the cumulative P-wave radiation (a: 0.003–1.0 Hz; b: 0.02–0.1 Hz; c: 0.03–0.3 Hz; d: 0.05–0.5 Hz; e: 0.1–1.0 Hz; f: 0.3–2.0 Hz), the aftershock distribution, and the largest aftershock (Mw 7.8) on September 18, 2025. White contour lines show the depth of the subducting slab in this region (Hayes et al., 2018). Black dots correspond to aftershocks (M ≥ 4.0; extracted from the USGS catalog) that occurred within two weeks after the Mw 8.8 mainshock. Yellow and red stars indicate the epicenter of Mw 8.8 and 7.8 earthquakes, respectively. Black and magenta lines show BP results for the Mw 7.8 aftershock, representing the 25% contour lines of P-wave radiation power for 0.05–0.5 Hz and 0.1–1.0 Hz, respectively.

1998; Gabuchian et al., 2017).

4.3. P-wave radiation area and aftershocks

Fig. 7 shows the spatial relationship between the cumulative P-wave radiation and the aftershock distribution within two weeks after the mainshock. The cumulative radiation area of the largest aftershock (Mw 7.8) on September 18, 2025 is also superimposed as black (0.05-0.5 Hz) and magenta (0.1-1.0 Hz) contours in Fig. 7. The BP results for this Mw 7.8 event are presented in the Supplementary Material (Fig. S6).

The aftershock distribution mostly overlaps the P-wave radiation area of the Mw 8.8 main-

shock, supporting the spatial extent of our BP-derived source region (Fig. 7). The Mw 7.8 aftershock radiated P-waves from the northern part of the source region, outside the main rupture zone on July 29, as indicated by the aftershock distribution (Figs. 7 and S8). This observation suggests that the Mw 8.8 event may have promoted failure in the northern segment, which subsequently generated the largest aftershock.

Aftershocks are concentrated around the LF source areas, whereas very few events occur near the strongest HF patches (Fig. 7). The LF source areas generally correspond to regions of large slip and long-duration rupture associated with substantial stress drop, which can suppress aftershock occurrence within the main patches with large slip and instead concentrate aftershocks around their margins (Wetzler et al., 2018). A comparison between our BP results and the aftershock locations shows that the shallow near-trench episodes E1 and E3, well resolved in the relatively higher LF bands (0.03–0.3 Hz and 0.05–0.5 Hz; Figs. 4(b, c) and 7(c, d)), are consistent with this interpretation. The HF source distributions exhibit a similar tendency (Fig. 7), implying that intense HF emission may reflect large local stress changes. In contrast, the E2 region, highlighted in the lowest-frequency band (0.02–0.1 Hz; Fig. 4(a)), does not follow the asperity-related aftershock pattern proposed by Wetzler et al. (2018). According to Bürgmann et al. (2005), the slip-deficit rate in the E2 region is higher than in any other part of the offshore Kamchatka area, suggesting that this segment did not fully release the shear strain accumulated since the 1952 event.

4.4. Relationship with historical events

The Kamchatka Peninsula has repeatedly experienced great earthquakes, including events in 1737, 1792, 1841, 1923, and 1952 (e.g., Johnson and Satake, 1999; MacInnes et al., 2010; Pinegina et al., 2018). The rupture characteristics of the 1952 event have been investigated in several studies (Ben-Menahem and Toksöz, 1963; Kanamori, 1976; Johnson and Satake, 1999; MacInnes et al., 2010). These studies consistently infer southwestward rupture propagation from the epicenter, similar to the 2025 event. Johnson and Satake (1999) estimated large slip at depth beneath southern Kamchatka and Paramushiru from historical tsunami records, whereas MacInnes et al. (2010)

allowed for alternative scenarios involving significant shallow slip to account for the tsunami deposits.

Our BP model (Figs. 3 and 4) provides a complementary perspective to the tsunami-based inversion of Johnson and Satake (1999). Because Johnson and Satake (1999) did not incorporate the coupling between tsunamis and a self-gravitating, deformable Earth (Watada et al., 2014) in their Green's functions, their inferred slip distribution was concentrated on deeper fault patches (e.g., Yagi et al., 2025). In line with the interpretation of MacInnes et al. (2010), our P-wave radiation pattern extends into the main source region of the 1952 M_w 9.0 event; in particular, episode E3 in southeastern Kamchatka is consistent with a major slip patch inferred from tsunami deposits (MacInnes et al., 2010).

Geological studies indicate that the 1737 event was likely the largest among these historical earthquakes, based on tsunami deposits (Pinegina et al., 2018, 2020). The 2025 M_w 8.8 earthquake, as inferred from its P-wave radiation images and inversion studies (Yagi et al., 2025; USGS, 2025b), appears comparable to the 1952 earthquake, suggesting that the recent megathrust rupture reactivated a source region similar to that of the 1952 event. This, in turn, may imply that the 1952 great earthquake did not fully release the shear strain that had accumulated since 1737.

5. Conclusions

We performed a multi-frequency teleseismic P-wave back-projection (BP) analysis of the 2025 M_w 8.8 Kamchatka earthquake using six frequency bands. Our BP images reveal four distinct episodes within the first 180 s, during which the rupture migrated southwestward, including two prominent shallow, near-trench P-wave radiation episodes. Our findings demonstrate that multi-frequency P-wave BP provides a useful framework for characterizing the depth- and frequency-dependent rupture behavior of the great subduction earthquake, as summarized below:

1. Low-frequency (LF) P-wave radiation highlights shallow, near-trench sources (E1 and E3), whereas high-frequency (HF) one emphasizes deeper sources in the initial and mid-sequence

phases (E0, deeper E2) and reveals an additional patch (E3′) along the downdip edge of the near-trench E3 source.

2. HF P-wave bursts coincide with accelerations in the expansion of the LF radiating region and its leading edges, possibly reflecting the abrupt changes in rupture and slip velocities.
3. E3 captures the shallow P-wave radiation near the trench, which may reflect dynamic overshoot.
4. Aftershocks concentrate around the LF-dominated E2 region, whereas they are sparse around the intense HF radiation patches. In contrast, the E2 region, despite its LF radiation, coincides with a segment of high slip-deficit rate and appears to have retained significant shear strain.

Acknowledgments

All seismograms used in this study were downloaded from the EarthScope Data Management Center (https://ds.iris.edu/ds/nodes/dmc/). We used ObsPy (Beyreuther et al., 2010) for seismic waveform analysis and data acquisition. To generate the figures, we used matplotlib (Hunter, 2007), cartopy (Office, 2010), Generic Mapping Tools (Wessel et al., 2019), and PyGMT (Uieda et al., 2021). In this study, we employed earthquake catalogs by Global CMT (Ekström et al., 2012).

Data Availability

All seismograms used in this study are available from the EarthScope Data Management Center (https://ds.iris.edu/ds/nodes/dmc/).

References

Ben-Menahem, A., Toksöz, M.N., 1963. Source mechanism from spectrums of long-period surface waves: 2. the kamchatka earthquake of november 4,1952. Journal of Geophysical Research 68, 5207–5222. doi:10.1029/jz068i018p05207.

Beyreuther, M., Barsch, R., Krischer, L., Megies, T., Behr, Y., Wassermann, J., 2010. ObsPy: A python toolbox for seismology. Seismological Research Letters 81, 530–533. doi:10.1785/gssrl.81.3.530.

Bürgmann, R., Kogan, M.G., Steblov, G.M., Hilley, G., Levin, V.E., Apel, E., 2005. Interseismic coupling and asperity distribution along the kamchatka subduction zone. Journal of Geophysical Research: Solid Earth 110. doi:10.1029/2005jb003648.

Dhakal, A.S., Molinari, I., Boschi, L., 2022. Seismic source mapping by surface wave time reversal: application to the great 2004 sumatra earthquake. Geophysical Journal International doi:10.1093/gji/ggac493.

Dziewonski, A.M., Chou, T., Woodhouse, J.H., 1981. Determination of earthquake source parameters from waveform data for studies of global and regional seismicity. Journal of Geophysical Research: Solid Earth 86, 2825–2852. doi:10.1029/jb086ib04p02825.

Ekström, G., Nettles, M., Dziewoński, A., 2012. The global CMT project 2004–2010: Centroid-moment tensors for 13,017 earthquakes. Physics of the Earth and Planetary Interiors 200, 1–9. doi:10.1016/j.pepi.2012.04.002.

Emelyanova, A., 2025. A 15-meter tsunami sends people and seals into panic. what's known about the kamchatka earthquake that reached the US and chile? (in russian). URL: https://www.fontanka.ru/2025/07/30/75782941/.

Fukahata, Y., Yagi, Y., Rivera, L., 2014. Theoretical relationship between back-projection imaging and classical linear inverse solutions. Geophysical Journal International 196, 552–559. doi:10.1093/gji/ggt392.

Gabuchian, V., Rosakis, A.J., Bhat, H.S., Madariaga, R., Kanamori, H., 2017. Experimental evidence that thrust earthquake ruptures might open faults. Nature 545, 336–339. doi:10.1038/nature22045.

Hayes, G.P., Moore, G.L., Portner, D.E., Hearne, M., Flamme, H., Furtney, M., Smoczyk, G.M., 2018. Slab2, a comprehensive subduction zone geometry model. Science (New York, N.Y.) 362, 58–61. doi:10.1126/science.aat4723.

Hunter, J.D., 2007. Matplotlib: A 2d graphics environment. Computing in Science & Engineering 9, 90–95. doi:10.1109/mcse.2007.55.

Ide, S., Baltay, A., Beroza, G.C., 2011. Shallow dynamic overshoot and energetic deep rupture in the 2011 mw 9.0 tohoku-oki earthquake. Science 332, 1426–1429. doi:10.1126/science.1207020.

Ishii, M., 2011. High-frequency rupture properties of the mw 9.0 off the pacific coast of tohoku earthquake. Earth, Planets and Space 63, 18. doi:10.5047/eps.2011.07.009.

Ishii, M., Shearer, P.M., Houston, H., Vidale, J.E., 2005. Extent, duration and speed of the 2004 sumatra–andaman earthquake imaged by the hi-net array. Nature 435, 933–936. doi:10.1038/nature03675.

Ishii, M., Shearer, P.M., Houston, H., Vidale, J.E., 2007. Teleseismic p wave imaging of the 26 december 2004

sumatra-andaman and 28 march 2005 sumatra earthquake ruptures using the hi-net array. Journal of Geophysical Research: Solid Earth (1978–2012) 112. doi:10.1029/2006jb004700.

Johnson, J.M., Satake, K., 1999. Asperity distribution of the 1952 great kamchatka earthquake and its relation to future earthquake potential in kamchatka. pure and applied geophysics 154, 541–553. doi:10.1007/s000240050243.

Kanamori, H., 1976. Re-examination of the earth's free oxcillations excited by the kamchatka earthquake of november 4, 1952. Physics of the Earth and Planetary Interiors 11, 216–226. doi:10.1016/0031-9201(76)90066-2.

Kennett, B.L.N., Engdahl, E.R., Buland, R., 1995. Constraints on seismic velocities in the earth from traveltimes. Geophysical Journal International 122, 108–124. doi:10.1111/j.1365-246x.1995.tb03540.x.

Kiser, E., Ishii, M., 2013. Hidden aftershocks of the 2011 mw 9.0 tohoku, japan earthquake imaged with the backprojection method. Journal of Geophysical Research: Solid Earth 118, 5564–5576. doi:10.1002/2013jb010158.

Koper, K.D., Hutko, A.R., Lay, T., Ammon, C.J., Kanamori, H., 2011. Frequency-dependent rupture process of the 2011 mw 9.0 tohoku earthquake: Comparison of short-period p wave backprojection images and broadband seismic rupture models. Earth, Planets and Space 63, 16. doi:10.5047/eps.2011.05.026.

MacInnes, B.T., Weiss, R., Bourgeois, J., Pinegina, T.K., 2010. Slip distribution of the 1952 kamchatka great earthquake based on near-field tsunami deposits and historical records. Bulletin of the Seismological Society of America 100, 1695–1709. doi:10.1785/0120090376.

Mizutani, A., Yomogida, K., 2022. Back-projection imaging of a tsunami excitation area with ocean-bottom pressure gauge array data. Journal of Geophysical Research: Oceans doi:10.1029/2022jc018480.

Office, M., 2010. Cartopy: a cartographic python library with a matplotlib interface URL: https://scitools.org.uk/cartopy.

Oglesby, D.D., Archuleta, R.J., Nielsen, S.B., 1998. Earthquakes on dipping faults: The effects of broken symmetry. Science 280, 1055–1059. doi:10.1126/science.280.5366.1055.

Okuwaki, R., Yagi, Y., Hirano, S., 2014. Relationship between high-frequency radiation and asperity ruptures, revealed by hybrid back-projection with a non-planar fault model. Scientific Reports 4, 7120. doi:10.1038/srep07120.

Pinegina, T., Bourgeois, J., Bazanova, L., Zelenin, E., Krasheninnikov, S., Portnyagin, M., 2020. Coseismic coastal subsidence associated with unusually wide rupture of prehistoric earthquakes on the kamchatka subduction zone: A record in buried erosional scarps and tsunami deposits. Quaternary Science Reviews 233, 106171. doi:10.1016/j.quascirev.2020.106171.

Pinegina, T.K., Bazanova, L.I., Zelenin, E.A., Bourgeois, J., Kozhurin, A.I., Medvedev, I.P., Vydrin, D.S., 2018. Holocene tsunamis in avachinsky bay, kamchatka, russia. Pure and Applied Geophysics 175, 1485–1506. doi:10.

1007/s00024-018-1830-0.

Rost, S., Thomas, C., 2002. ARRAY SEISMOLOGY: METHODS AND APPLICATIONS: ARRAY SEISMOLOGY. Reviews of Geophysics 40, 2–1–2–27. doi:10.1029/2000rg000100.

Ruiz-Angulo, A., Melgar, D., Marez, C.d., Deniau, A., Nencioli, F., Hjörleifsdóttir, V., 2025. SWOT satellite altimetry observations and source model for the tsunami from the 2025 m 8.8 kamchatka earthquake. The Seismic Record 5, 341–351. doi:10.1785/0320250037.

Shimizu, K., Yagi, Y., Okuwaki, R., Fukahata, Y., 2019. Development of an inversion method to extract information on fault geometry from teleseismic data. Geophysical Journal International 220, 1055–1065. doi:10.1093/gji/ggz496.

Tarumi, K., Yoshizawa, K., 2023. Eruption sequence of the 2022 hunga tonga-hunga ha'apai explosion from back-projection of teleseismic p waves. Earth and Planetary Science Letters 602, 117966. doi:10.1016/j.epsl.2022.117966.

Tarumi, K., Yoshizawa, K., 2025. Frequency-dependent seismic radiation process of the 2024 noto peninsula earthquake from teleseismic p-wave back-projection. Earth and Planetary Science Letters 666, 119509. doi:10.1016/j.epsl.2025.119509.

Uieda, L., Tian, D., Leong, W.J., Jones, M., Schlitzer, W., Toney, L., Grund, M., Yao, J., Magen, Y., Materna, K., Newton, T., Anant, A., Ziebarth, M., Wessel, P., Quinn, J., 2021. PyGMT: A python interface for the generic mapping tools URL: https://doi.org/10.5281/zenodo.5607255, doi:10.5281/zenodo.5607255.

USGS, 2025a. M 7.8 - 138 km e of petropavlovsk-kamchatsky, russia. URL: https://earthquake.usgs.gov/earthquakes/eventpage/us7000qx2g/finite-fault.

USGS, 2025b. M 8.8 - 2025 kamchatka peninsula, russia earthquake. URL: https://earthquake.usgs.gov/earthquakes/eventpage/us6000qw60/executive.

Vinnik, L., 1977. Detection of waves converted from p to SV in the mantle. Physics of the Earth and Planetary Interiors 15, 39–45. URL: https://www.sciencedirect.com/science/article/pii/0031920177900085, doi:10.1016/0031-9201(77)90008-5.

Watada, S., Kusumoto, S., Satake, K., 2014. Traveltime delay and initial phase reversal of distant tsunamis coupled with the self-gravitating elastic earth. Journal of Geophysical Research: Solid Earth 119, 4287–4310. doi:10.1002/2013jb010841.

Wessel, P., Luis, J.F., Uieda, L., Scharroo, R., Wobbe, F., Smith, W.H.F., Tian, D., 2019. The generic mapping tools version 6. Geochemistry, Geophysics, Geosystems 20, 5556–5564. doi:10.1029/2019gc008515.

Wetzler, N., Lay, T., Brodsky, E.E., Kanamori, H., 2018. Systematic deficiency of aftershocks in areas of high

coseismic slip for large subduction zone earthquakes. Science Advances 4, eaao3225. doi:10.1126/sciadv.aao3225.

Yagi, Y., Fukahata, Y., 2011. Introduction of uncertainty of green's function into waveform inversion for seismic source processes. Geophysical Journal International 186, 711–720. doi:10.1111/j.1365-246x.2011.05043.x.

Yagi, Y., Fukahata, Y., Okuwaki, R., Takagawa, T., Toda, S., 2025. Breaking the cycle: Short recurrence and overshoot of an m9-class kamchatka earthquake. Seismica 4. doi:10.26443/seismica.v4i2.2012.

Yagi, Y., Nakao, A., Kasahara, A., 2012. Smooth and rapid slip near the japan trench during the 2011 tohoku-oki earthquake revealed by a hybrid back-projection method. Earth and Planetary Science Letters 355, 94–101. doi:10.1016/j.epsl.2012.08.018.

Yamashita, S., Yagi, Y., Okuwaki, R., Shimizu, K., Agata, R., Fukahata, Y., 2022. Potency density tensor inversion of complex body waveforms with time-adaptive smoothing constraint. Geophysical Journal International 231, 91–107. doi:10.1093/gji/ggac181.

Supplementary Material for

Multi-frequency Teleseismic P-wave Back-projection of the 2025 Mw 8.8 Kamchatka Peninsula Earthquake

K. Tarumi[1,*] and K. Yoshizawa[1]

[1] Department of Earth & Planetary Sciences, Faculty of Science, Hokkaido University, Sapporo 060-0810, Japan.

[*]Corresponding author: tarumi.kotaro.jp@gmail.com

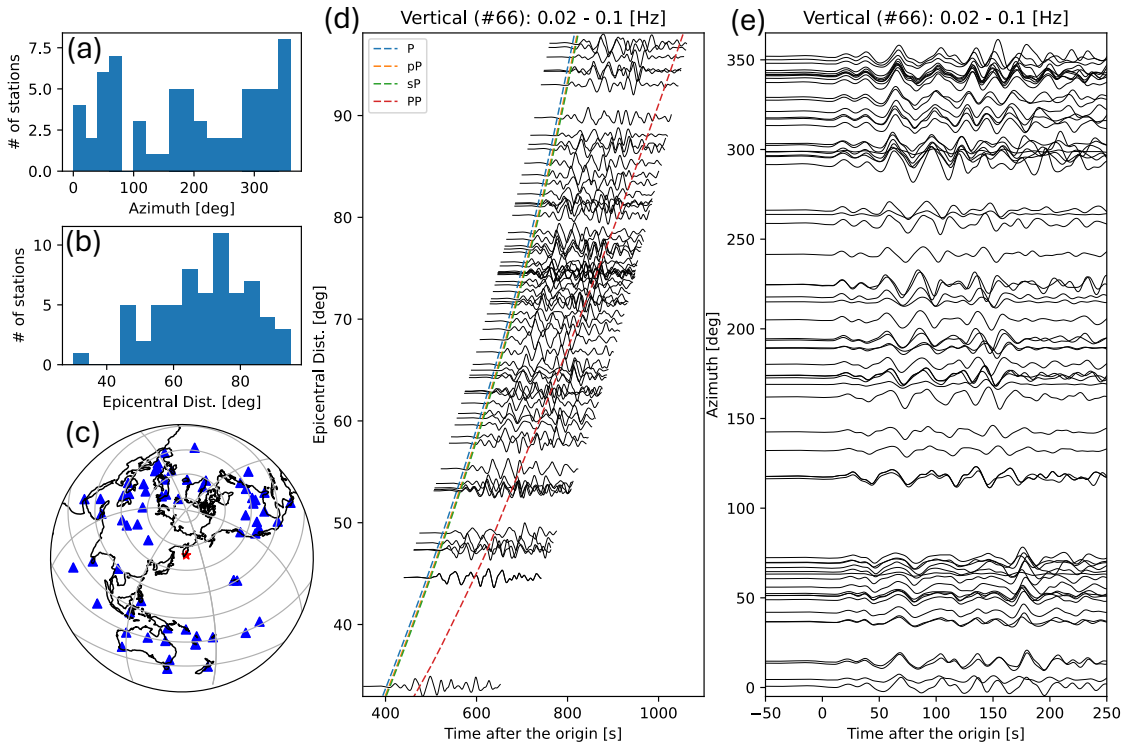

Figure S1: Same as Figure 2 in the main text, but for 0.02–0.1 Hz.

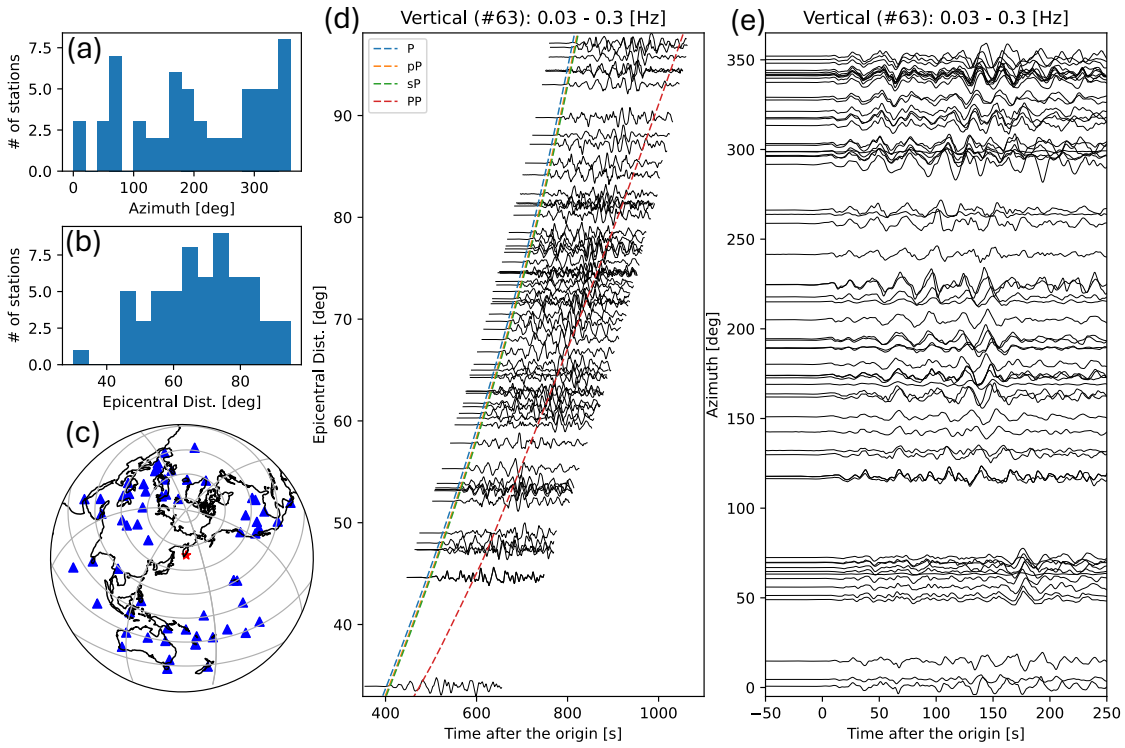

Figure S2: Same as Figure 2 in the main text, but for 0.03–0.3 Hz.

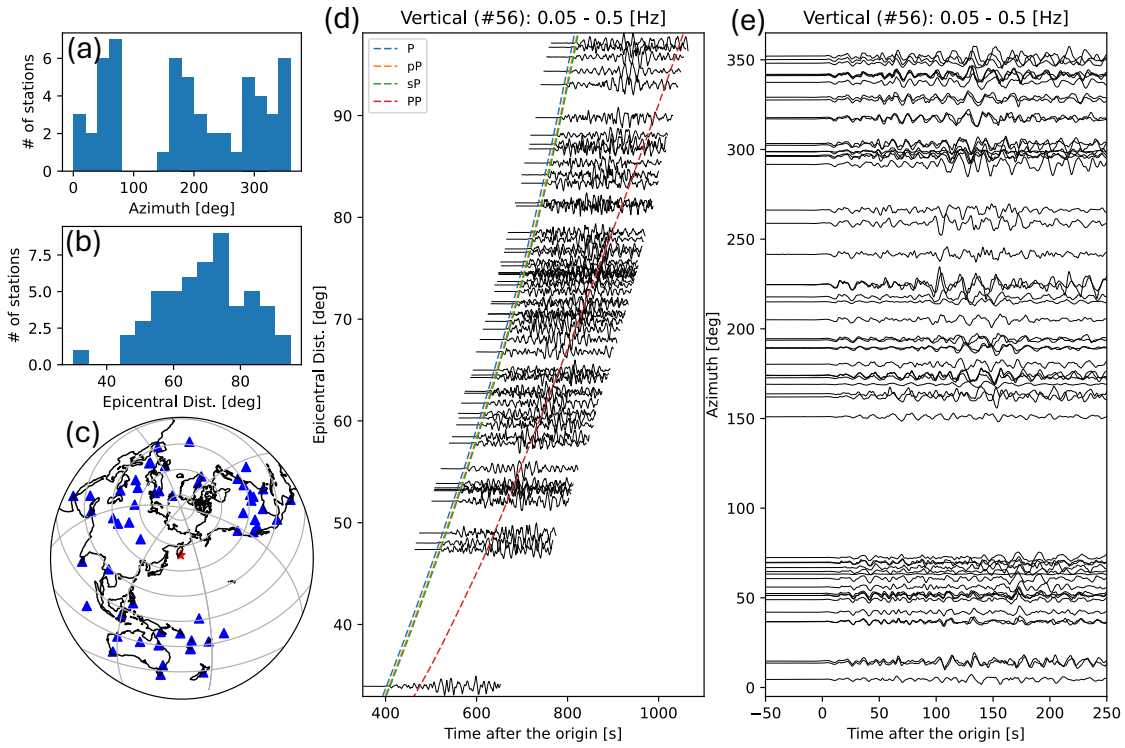

Figure S3: Same as Figure 2 in the main text, but for 0.05–0.5 Hz.

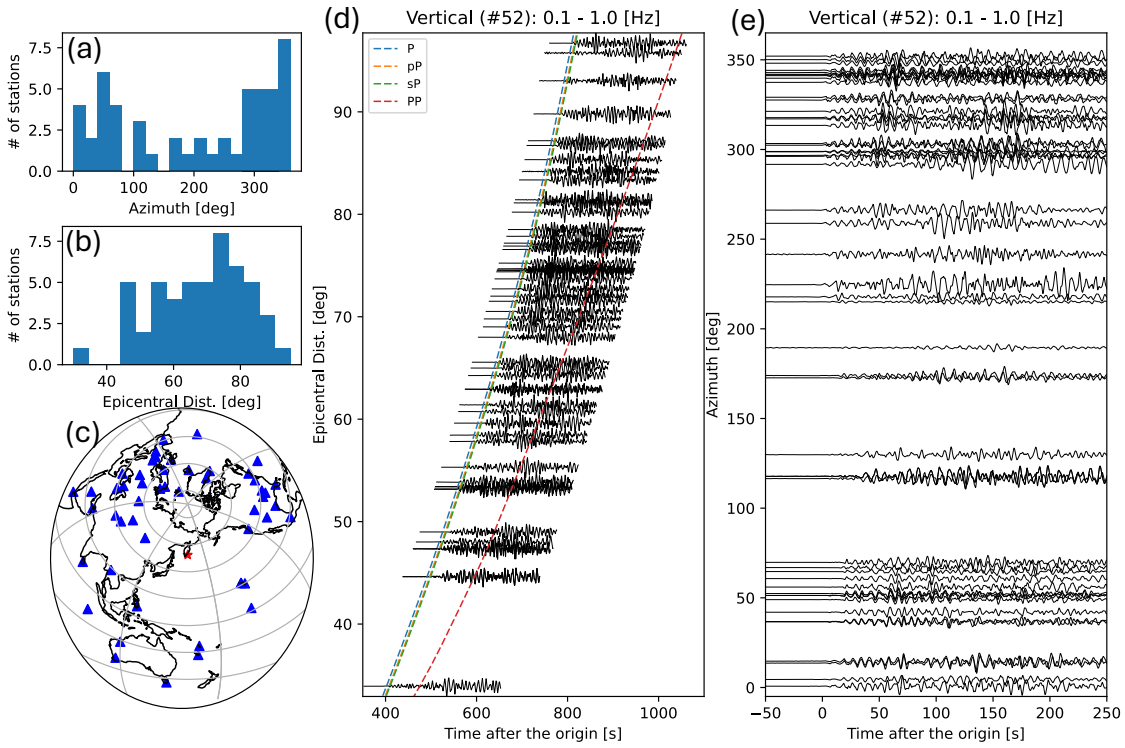

Figure S4: Same as Figure 2 in the main text, but for 0.1–1.0 Hz.

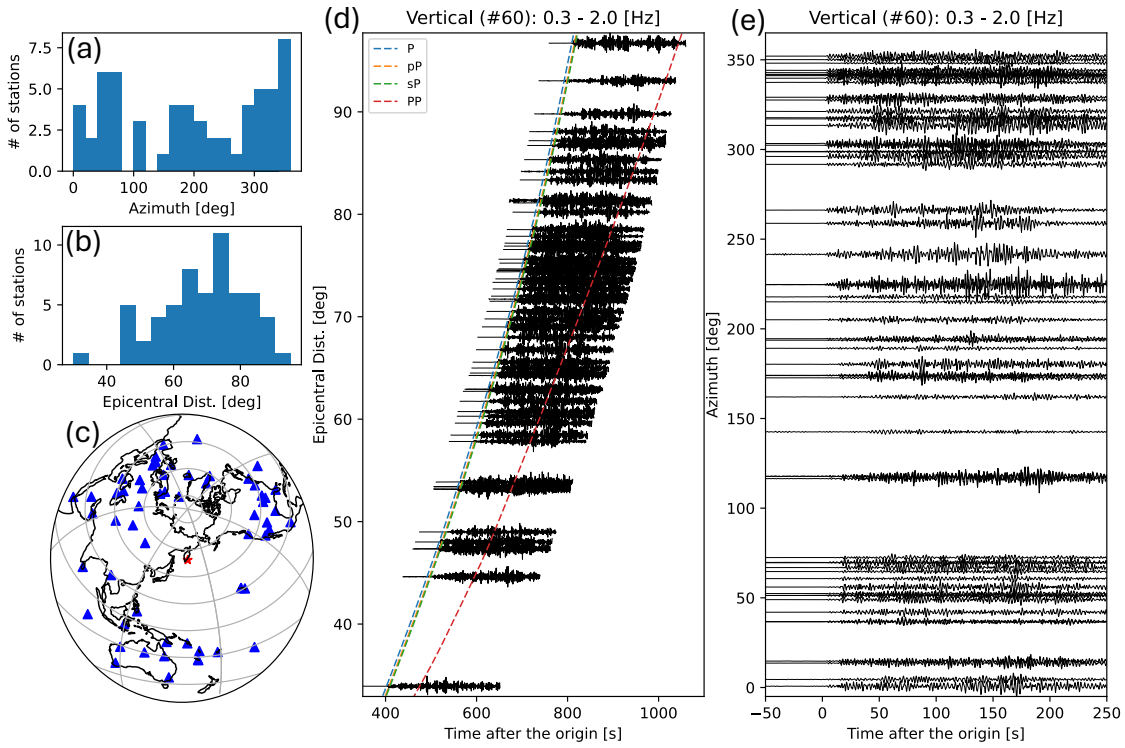

Figure S5: Same as Figure 2 in the main text, but for 0.3–2.0 Hz.

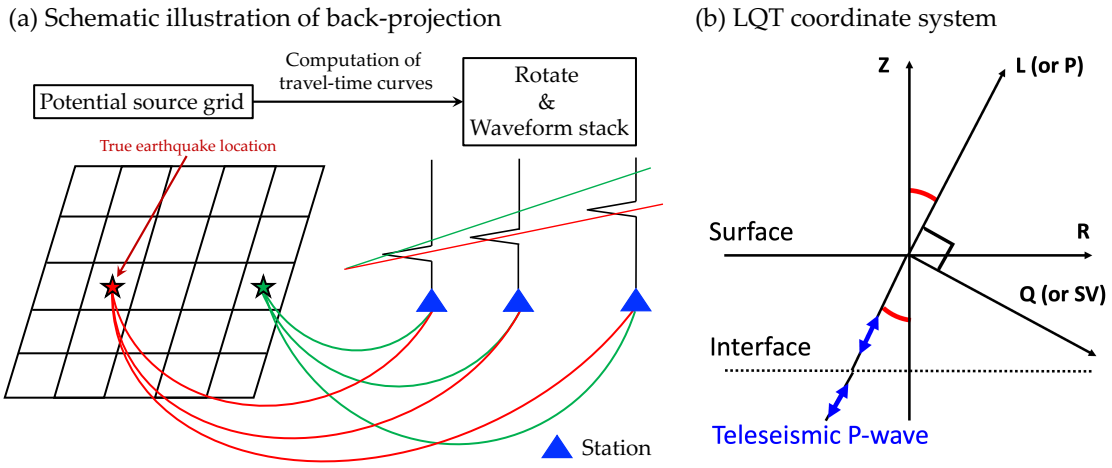

Figure S6: (a) Schematic illustration of the back-projection method. (b) LQT coordinate system.

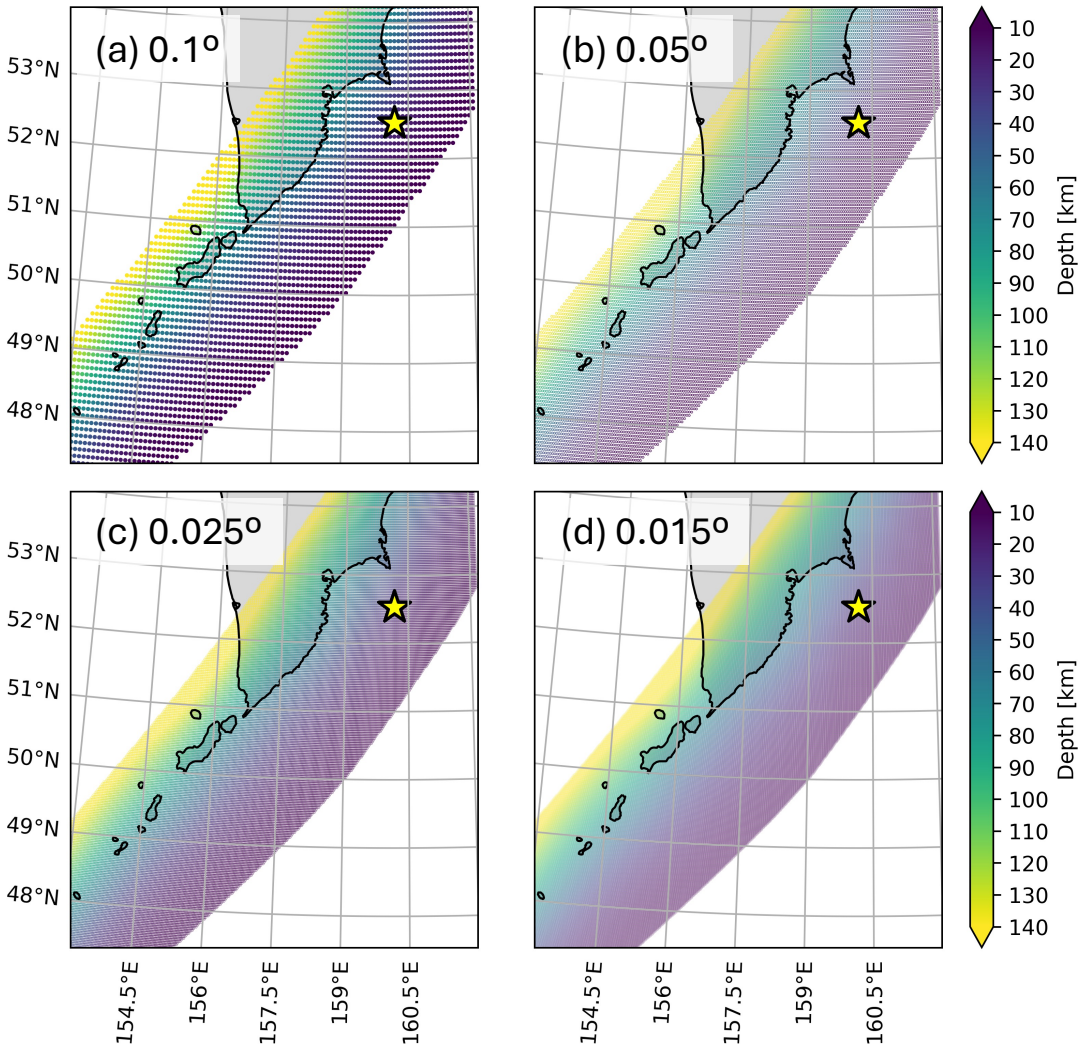

Figure S7: Potential source grids implemented for the BP process. Detailed descriptions of grid intervals are provided in Table 1. Yellow stars represent the epicenter of the 2025 Mw 8.8 Kamchatka earthquake.

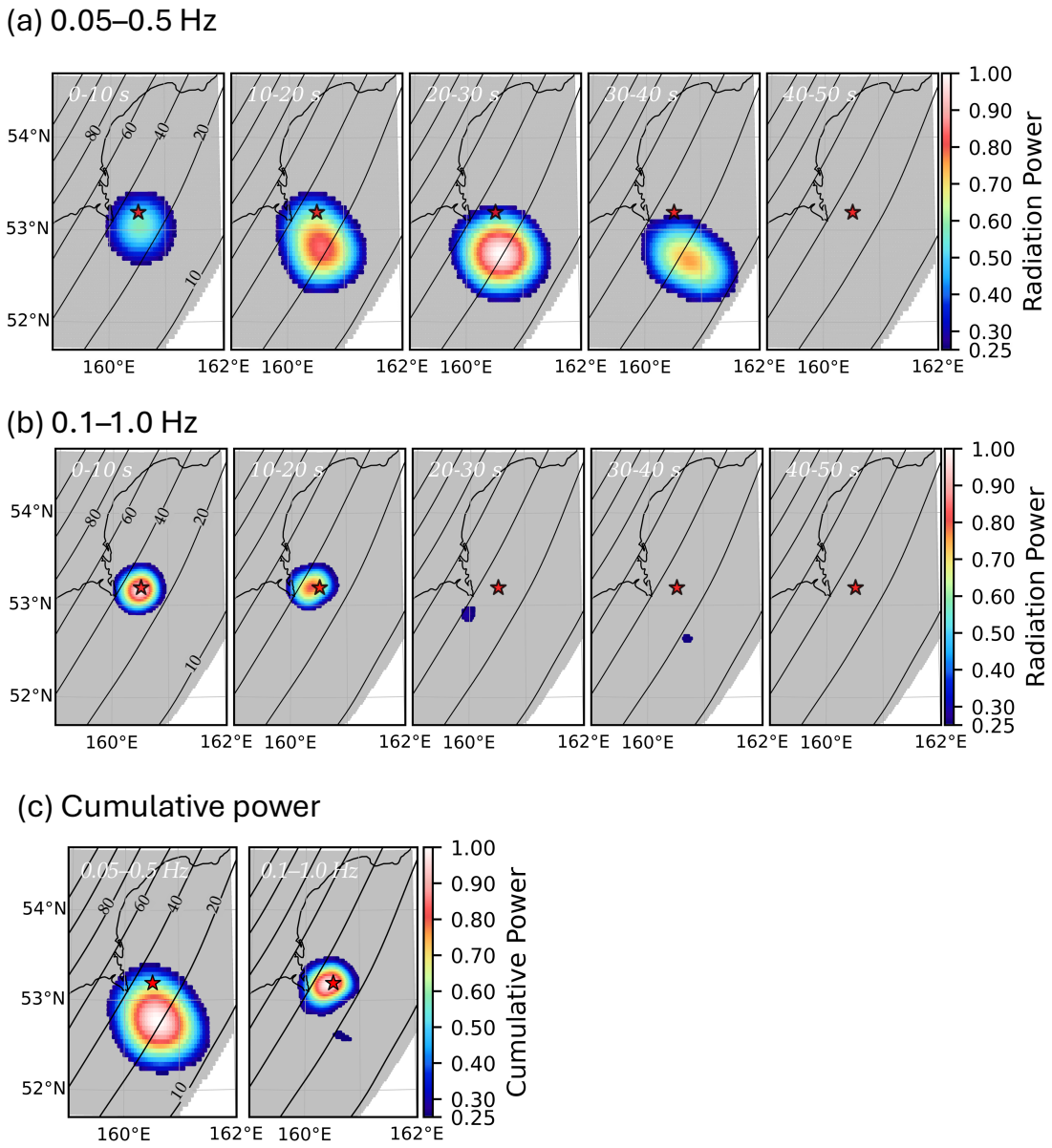

Figure S8: BP results for the largest aftershock with Mw 7.8 on September 18, 2025. (a, b) Snapshots of P-wave radiation power at 10-second intervals. The red star represents the epicenter of this aftershock. Black contour lines show the 10 km depth interval of the subducting plate extracted from the Slab 2.0 model. (c) Cumulative P-wave radiation power. Left and right panels correspond to 0.05–0.5 Hz and 0.1–1.0 Hz, respectively.